

Tailoring photoluminescence in MoSSe alloys through gold nanostructure coupling: Influence of midgap states and localized surface-plasmon resonance

Chumki Nayak,¹ Suvadip Masanta^{1,*}, Sanchi Monga,^{2,*} Swastik Paul³, Souhardya Bera,³ Shibshankar Mondal³, Saswata Bhattacharya^{2,†} and Achintya Singha^{1,‡}

¹*Department of Physical Sciences, Bose Institute, 93/1, Acharya Prafulla Chandra Road, Kolkata 700 009, India*

²*Department of Physics, Indian Institute of Technology Delhi, New Delhi 110016, India*

³*Department of Chemical Engineering, University of Calcutta, 92, Acharya Prafulla Chandra Road, Kolkata 700 009, India*



(Received 21 November 2023; accepted 21 February 2024; published 21 March 2024)

Tuning exciton-plasmon interaction in transition metal dichalcogenides coupled with noble metal nanostructures has emerged as a powerful technique with broad implications in the fields of cavity quantum electrodynamics, spintronics, valleytronics, etc. Here, we report a simple strategy to modulate recombination pathways in the emerging transition metal dichalcogenide alloy MoSSe coupled with Au nanoclusters by engineering the geometrical parameters of Au nanoclusters. Systematic investigations using photoluminescence spectroscopy were performed on Au/MoSSe hybrids under 488 nm excitation. Our results demonstrate Au size-dependent quenching to the subsequent enhancement of the MoSSe emission within the same hybrid system. First-principles calculations provide a microscopic understanding of the presence of the midgap state in the hybrid system leading to the quenching phenomenon. Additionally, the evolution of the Au nanoclusters' geometry induces local surface-plasmon resonance, which eventually enhances the photoluminescence intensities of the hybrid system, in agreement with theoretical calculations. Excitation with a laser of energy close to the emission of Au nanoclusters leads to a significant modification of the photoluminescence emission of the hybrids compared to the previous one. The modulation of the absorption and vibrational properties of the Au/MoSSe hybrid system further supports the findings from the photoluminescence studies. This comprehensive study provides valuable insights into the metal-transition metal dichalcogenide interface, thereby contributing to an improved understanding of the underlying mechanism. Furthermore, the demonstrated potential of this approach presents a promising avenue for the development of novel broadband optoelectronic designs.

DOI: [10.1103/PhysRevB.109.125306](https://doi.org/10.1103/PhysRevB.109.125306)

I. INTRODUCTION

Tailoring light-matter interaction in two-dimensional (2D) materials has led to remarkable advancements in the field of optoelectronics [1,2]. Among the extensive group of layered 2D materials, semiconducting transition metal dichalcogenides (TMDCs) have garnered substantial attention for both fundamental research and practical applications [3,4]. TMDCs possess favorable properties as active materials due to their superior excitonic behavior [5,6]. However, the photoluminescence (PL) quantum yield is significantly affected by low carrier recombination, which stems from the short exciton lifetime and strong exciton-exciton interaction at room temperature [7,8]. Additionally, the narrow spectral window limits their applications in photonic devices [9,10]. Consequently, the exploration of strategies to enhance the optoelectronic potential of TMDCs by addressing these challenges through chemical modification, defect engineering, and hybridization has emerged as a captivating area of research [11–15].

In this regard, integration with plasmonic nanostructures offers a promising avenue for tuning and enhancing excitonic behavior in TMDCs [16–19]. The interaction between excitons and plasmons can lead to significant changes in the optical and vibrational properties of the active material. By modifying the size, shape, and thickness of metal nanostructures, the exciton-plasmon pathway in plasmonic metal nanostructure/TMDC hybrid systems can be tailored, thereby altering the rates of radiative and nonradiative recombination. This approach holds great potential for engineering highly efficient hybrid nanodevices in the field of photosensing [20–22]. This interplay is governed by two fundamental phenomena: charge transfer and localized surface-plasmon resonance (LSPR). Previous studies reported on the hybrid plasmonic nanoparticle (NP)/TMDC behaviors arising out of energy or charge transfer or LSPR, thereby leading to either quenching or enhancement of PL emission [23–28]. To the best of our knowledge, there is one report that investigated the enhancement and quenching regimes in CdSe coupled to Au NP [29]. However, the microscopic dynamics of charge transfer and carrier recombination and their potential impact on optical properties still remain unclear. Furthermore, there is a lack of contemporary investigation on hybrid systems. In the present study, an emerging TMDC alloy, molybdenum sulfoselenide (MoSSe), is chosen due to its rich near-infrared

*These authors contributed equally to this work.

†Corresponding author: saswata@physics.iitd.ac.in

‡Corresponding author: achintya@jcbose.ac.in

(NIR) efficiency [30]. We adopt a general approach to coupling plasmonic nanostructures with MoSSe to demonstrate subsequent quenching and enhancement of optical emissions in a single hybrid system by modulating the geometry of the nanostructures. Thus, the plasmon/MoSSe hybrid system will have critical importance in providing a comprehensive microscopic understanding through a combined systematic investigation of experimental and theoretical studies.

Here, a series of Au/MoSSe hybrids were fabricated by varying the sizes of Au nanoclusters (NCs). The integration of Au NCs with MoSSe enabled broadband absorption ranging from the UV-visible (VIS) to NIR region, effectively addressing the limited spectral window issue. Experimental investigations using PL and Raman studies demonstrated successful tuning of the optical and vibrational properties of MoSSe through the incorporation of Au NCs. First-principles calculations further provided microscopic understanding about Au/MoSSe hybrid samples, after the incorporation of Au NCs. The observed quenching in PL emission was attributed to the formation of midgap states during the initial phases of Au growth over the MoSSe layer, leading to nonradiative charge recombination. Subsequent band realignment in the hybrid structure facilitated charge transfer from MoSSe to Au NCs. By systematically modifying the geometry of Au NCs, the localized electric field resulting from surface-plasmon resonance (SPR) played a pivotal role in increasing the PL intensity. Consequently, the metal-TMDC interface, a critical factor in optoelectronic device design, can be easily modulated. This work provides both experimental and theoretical groundwork for the development of next-generation optoelectronic devices, such as photodetectors, solar cells, and light-emitting devices, based on plasmonic nanostructures coupled with alloy TMDC materials.

II. EXPERIMENT

A. Material synthesis

The MoSSe crystal was purchased from HQ Graphene, the Netherlands. We adopted the mechanical exfoliation route by the standard scotch-tape method to get monolayer and few-layer samples on a SiO₂ (thickness = 300 nm)/doped Si substrate. To prepare the Au/MoSSe hybrid samples, Au was deposited on pristine MoSSe (Sample 1) for 30 s (Sample 2), 50 s (Sample 3), 70 s (Sample 4), 100 s (Sample 5), 130 s (Sample 6), and 150 s (Sample 7) in a vacuum physical vapor deposition growth chamber (pressure $\sim 10^{-3}$ Torr). For the absorption study, we also prepared Au NCs on MoSSe using a glass slide as the substrate using the same method (see the Supplemental Material [31], Sec. VII).

B. Material characterizations

To understand the topography of the samples, atomic force microscopy (AFM) images were taken in the tapping mode using a Bruker instrument (Innova). To study the vibrational and optical properties, Raman and PL measurements were performed using a micro-Raman setup equipped with a spectrometer (LabRAM HR, Jobin Yvon) and a Peltier-cooled CCD detector. An air-cooled argon-ion laser with a wavelength of 488 nm and a He-Ne laser with a wavelength

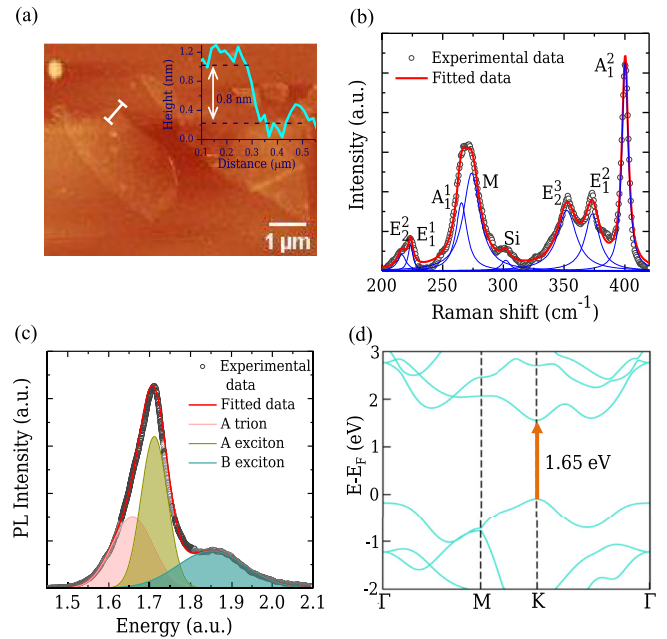


FIG. 1. Primary characterizations of pristine MoSSe (Sample 1). (a) AFM image (inset shows the height profile), (b) Raman spectrum, and (c) PL spectrum of Sample 1. (d) Calculated electronic band structure of monolayer MoSSe via DFT.

of 633 nm were used as excitation sources. The laser light was focused on the sample using a 100 \times objective with a numerical aperture of 0.9. To measure the optical absorption spectra of Au NCs and Au/MoSSe hybrids, we used a UV-VIS spectrophotometer from Perkin Elmer (Lambda 35). The theoretical band structures were calculated using density functional theory (DFT), and the computational details are provided in Sec. I of the Supplemental Material [31]. We performed the simulation using the COMSOL MULTIPHYSICS program.

III. RESULTS AND DISCUSSIONS

The details of the Au/MoSSe hybrid synthesis procedures are given in the previous section. Our as-prepared pristine MoSSe (Sample 1) is a monolayer, as confirmed by the AFM imaging shown in Fig. 1(a) (the height profile is given in the inset). Figure 1(b) represents the Raman spectrum of Sample 1. The most prominent Raman peaks are the E_2^2 , E_1^1 , A_1^1 , M , E_2^3 , E_1^2 , and A_2^1 modes, appearing at 216, 223, 265, 274, 352, 373, and 400 cm^{-1} , respectively, which is consistent with previous reports [30,32]. The PL spectrum shown in Fig. 1(c) is determined by exciton and trion recombination. The energies associated with the A trion, A exciton, and B exciton are 1.65, 1.7, and 1.86 eV, respectively. The calculated band structure of the pristine MoSSe monolayer shows that it is a direct band gap semiconductor with a band gap of 1.65 eV. The valence band maxima (VBM) and conduction band minima (CBM) of MoSSe lie at the K point in the irreducible Brillouin zone as depicted in Fig. 1(d), which is nearly equal to the excitonic band gap of MoSSe. Figure S1 shows the projected density of states (pDOS) plot of the pristine MoSSe monolayer, which reveals that the states near the VBM and CBM are primarily

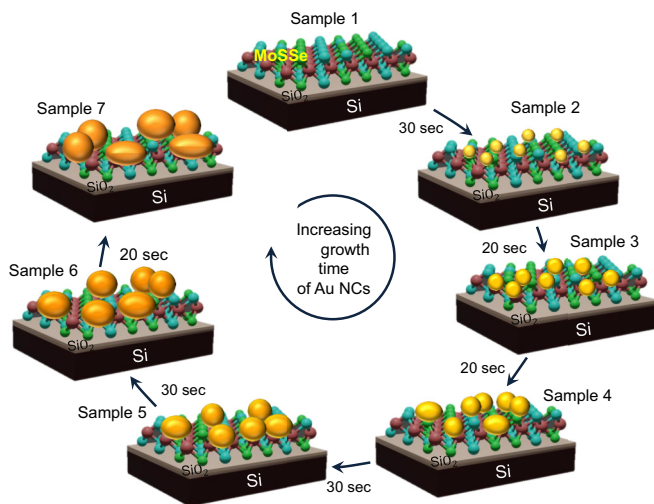


FIG. 2. Schematic representation of the synthesis steps of Au/MoSSe hybrids.

contributed by Mo *d* orbitals, with a small contribution from other orbitals [31].

Figure 2 shows a schematic representation of Au/MoSSe hybrid formation at successive growth times of Au NCs. The shape and size depicted are purely for illustrative purposes and to convey the dynamic evolution of the Au NCs as a function of time. Figures S2(a)–S2(c) represent AFM images of bare MoSSe (Sample 1) and Au/MoSSe hybrids at two different growth stages (Samples 3 and 5), where the insets show zoomed-in views of the regions outlined by rectangular boxes [31]. The line profiles of the AFM images illustrating the top surfaces of Samples 1, 3, and 5 are depicted in Fig. S2(d) [31]. The increased intensity of each peak in the line profile with the increase in Au deposition time suggests a corresponding increase in NCs size, aligning with the size distribution histograms derived from their respective AFM images (Figs. S2(e) and S2(f) [31]). The narrowing gap between the peaks of the line profile with an increase in Au growth time (see Fig. S2(d) [31]) suggests a reduction in the gap between the Au NCs, implying an increase in the area coverage of the Au NCs. To validate this observation, we calculated the percentage of area coverage of Au NCs for Samples 3 and 5 from their AFM topography. The estimated values of area coverage for Samples 3 and 5 are 18% and 40%, respectively. This result shows that with the increase in Au growth time, the area coverage of the Au NCs also increases, which is consistent with the line profile analysis.

To explore the effect of the shape and size modulation of Au NCs on exciton-plasmon coupling, we studied our as-grown hybrid samples via PL spectroscopy under the excitation of the 488 nm laser. The key results of our work are shown in Fig. 3. After formation of Au/MoSSe hybrids (from Sample 2 to Sample 7), Fig. 3(a) confirms two additional peaks with the existing exciton and trion peaks of Sample 1 [Fig. 1(c)] in the higher-energy region (1.8 to 2.3 eV). These can be assumed to be emanating from the Au NCs. From samples with growth times of 70 s and higher, the high-energy spectra could not be fitted reliably. This observation allowed for the addition of a new peak before the B excitonic

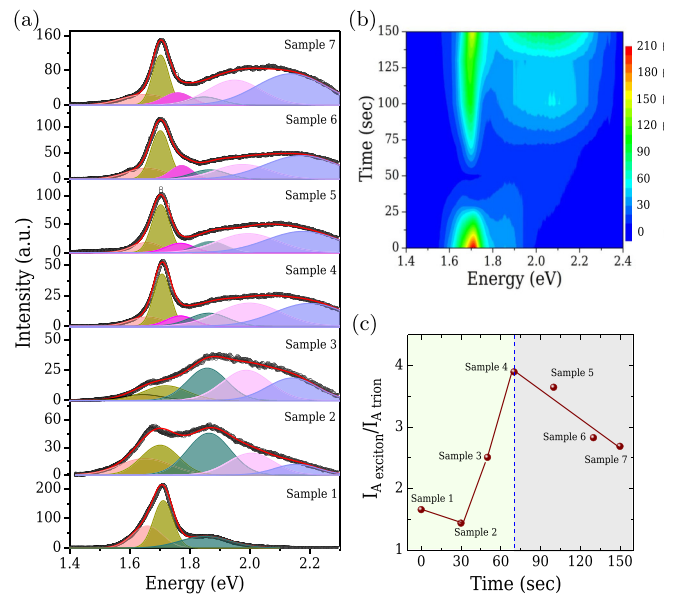


FIG. 3. Optical study of pristine MoSSe (Sample 1) and Au/MoSSe hybrids (Samples 2–7) under 488 nm laser excitation. (a) PL spectra of Samples 1–7. The red line represents the fitted curve. The spectra are fitted with four Gaussian functions corresponding to the A trion, A exciton, and B exciton for pristine MoSSe (Sample 1); two additional Gaussian fitted peaks for Au NCs (pink and violet) in hybrids (Samples 2–7); and a Gaussian fitted peak related to the B trion (magenta) for Samples 4–7. (b) Color plot of the PL intensity as a function of energy and Au growth time and (c) intensity ratio between the A exciton and A trion peaks for all samples.

transition, which is assigned as the B trion (magenta peak) [33–35]. To gain a comprehensive understanding of the aforementioned peaks subsequent to the formation of Au/MoSSe hybrids, it is essential to investigate the emission properties of the Au NCs. Therefore, the Au NCs were synthesized on a SiO₂ (thickness of 300 nm)/doped Si substrate, which is similar to the substrate used for Sample 1, over successive time segments like before. The PL emission of Au NCs is caused by the radiative recombination of *d*-band holes with *sp* electrons [36,37]. These PL spectra (Fig. S3(a) [31]) were fitted using two Gaussian functions which are comparable to the peaks appearing in the hybrid systems [Fig. 3(a)]. This observation confirms our assumption that the observed peaks beyond the emission of MoSSe in the hybrid samples originate from Au NCs. Between these two peaks, the lower-energy peak is assigned to the longitudinal mode, while the higher-energy peak is associated with the transverse mode (Fig. S3(a) [31]) [38,39]. With the evolution of the size of Au NCs with increasing growth time, both modes are slightly redshifted (Fig. S3(b) [31]), and their intensity increases (Fig. S3(c) [31]). Several recent reports showed the generation of the gap plasmon mode in metal-insulator-metal metasurfaces with a thin insulating layer [40–43]. However, in our case, a 300 nm thick layer of SiO₂ is placed between the Au NCs and doped Si. In the context of such a comparatively thick dielectric, the generation of a gap plasmon mode is not anticipated [42,44]. Therefore, the enhancement of PL intensity with the size

increment is attributed to the LSPR effect, which acts as an additional ultrafast radiative channel enhancing the radiative recombination of the interband transition of electrons and holes [45]. Now, coming back to the PL study of Au/MoSSe hybrid samples [Fig. 3(a)], it reveals an interesting observation.

Two distinct scenarios are observed in the experimental results. First, the intensity of peaks related to MoSSe decreases up to Sample 3. But from Sample 4, a significant and sharp rise in PL intensity is observed [Fig. 3(a)]. Conversely, the emission attributed to Au NCs shows an overall increase for all hybrid samples (Samples 2–7), as shown in Fig. S4(a) [31]. A comprehensive visualization of these observations is provided by the color plot in Fig. 3(b), which offers a clear overview of the overall behavior. Recently, Lu *et al.* reported the redshifting (15 nm) of the A exciton of Au NP/MoS₂ due to 0.4% strain present in the system [46]. In our study, the absence of a significant peak shift (Fig. S4(b) [31]) indicates that strain may not be a dominant factor influencing the optical properties in the hybrid system. Instead, we attribute the observed quenching effect to band realignment upon the formation of the hybrid structure, which facilitates charge transfer from MoSSe to Au NCs. As the growth time progresses, the evolution in size and density of Au NCs on MoSSe leads to the emergence of LSPR effects, which intensify the PL phenomena, countering the initial quenching. Consequently, the interplay between charge transfer and LSPR in the hybrid system results in both quenching and effective enhancement of optical emission, depending on the geometry of the Au NCs. However, the microscopic origin of both the quenching and enhancement phenomena remains yet to be fully elucidated. Here, the PL modification factor can be defined as

$$P_{\text{PL}} = \frac{I_{\text{Au/MoSSe}}}{I_{\text{MoSSe}}}, \quad (1)$$

where $I_{\text{Au/MoSSe}}$ and I_{MoSSe} are the PL intensities of MoSSe with and without the presence of Au NCs. The P_{PL} values for the A trion, A exciton, and B exciton decrease from 1 (Sample 1) to 0.03, 0.07, and 0.3 for Sample 3, where the maximum PL quenching of MoSSe occurs. Subsequently, they increase to 0.43, 0.67, and 0.33, respectively, for Sample 7 (Fig. S4(c) [31]). It is also observed that the intensity ratio of the A exciton to the A trion [Fig. 3(c)] first increases, and then after a certain Au growth time (after Sample 4), it decreases. Thus, the conversion of excitons to trions is directly influenced by the suppression of charge transfer. Interestingly, upon excitation with a 633 nm laser, there is very significant enhancement in PL emission peaks after Sample 4. The maximum P_{PL} (2.6 and 3.6 for the exciton and A trion, respectively) is achieved for Sample 7, as shown in Fig. 4(a). The resonance of the longitudinal mode of Au NCs (see Fig. S3(b) [31]) with excitation energy (1.96 eV) causes strong exciton-plasmon coupling which effectively amplifies the local surface-plasmon effect. However, due to the mismatch between the energy (2.54 eV) associated with the 488 nm excitation and the peaks of Au NCs, we observe a lower P_{PL} value (Fig. S4(c) [31]). Additionally, the high exciton to trion switching in the case of the 633 nm excitation [Fig. 4(b)] compared to the 488 nm excitation [Fig. 3(c)]

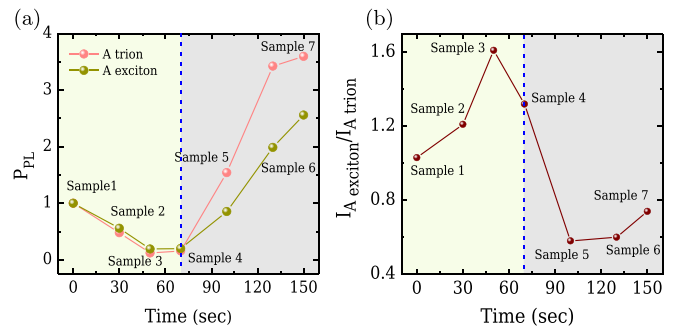


FIG. 4. Optical study of pristine MoSSe (Sample 1) and Au/MoSSe hybrids (Samples 2–7) under 633 nm laser excitation. (a) PL modification factor for the A exciton and A trion peaks and (b) the intensity ratio between the A exciton and A trion peaks for all samples.

is due to enhanced conversion of the exciton to a trion by excess photoinduced carriers at SPR conditions [47]. It must be mentioned that the SPR might activate the emission related to the B trion in the hybrid systems.

We conducted a systematic study of PL on two additional samples, MoSSe 2 and MoSSe 3, both of which are few-layer samples, as confirmed by the color contrast observed in optical microscopic images, PL intensity, and peak shift (see the Supplemental Material [31], Sec. VI). In both samples, the behavior regarding the change in PL intensity upon Au growth is qualitatively similar to that observed in the Au/monolayer MoSSe hybrid. However, the rate of revival of MoSSe peaks differs from that of Au/monolayer MoSSe hybrids (see Fig. S5(f), top panel [31]). Additionally, as observed in Fig. S5(f) (bottom panel) [31], the conversion of excitons to trions is less efficient compared to that of Au/monolayer MoSSe hybrids. The reason is that monolayer MoSSe exhibits a higher PL quantum yield than the few-layer samples due to its smaller crystal volume, significant quantum confinement, and reduced dielectric screening [5,6,25,28]. Consequently, efficient light-matter interaction is observed in monolayer MoSSe compared to few-layer samples, particularly with the geometric modulation of Au NCs in the hybrid systems.

To understand the quenching and enhancement scenarios mentioned above, we conducted a comprehensive study of the UV-VIS absorption properties for both Au NCs and Au/MoSSe hybrids using a glass slide as a substrate, as shown in Fig. S6 [31]. The observed absorption peak (Figs. S6(a) and S6(b) [31]) at 530 nm for both the samples (30 s Au NCs and Sample 2) can be attributed to the transverse mode of Au NCs [39,48]. The redshift of the absorption energy as the Au growth time increases can be attributed to the reduction in confinement energy [49]. This reduction arises from the formation of larger NCs, as validated by the AFM analysis (Figs. S2(d)–S2(f) [31]). Moreover, an additional peak around 650 nm emerges in the samples with longer growth times (Figs. S6(a) and S6(b) [31]), corresponding to the coupled plasmon resonance band [39,50], namely, the longitudinal absorption mode of Au. The appearance of this band and increase of the absorption intensity with the Au growth time indicate higher surface coverage [50], which is supported by

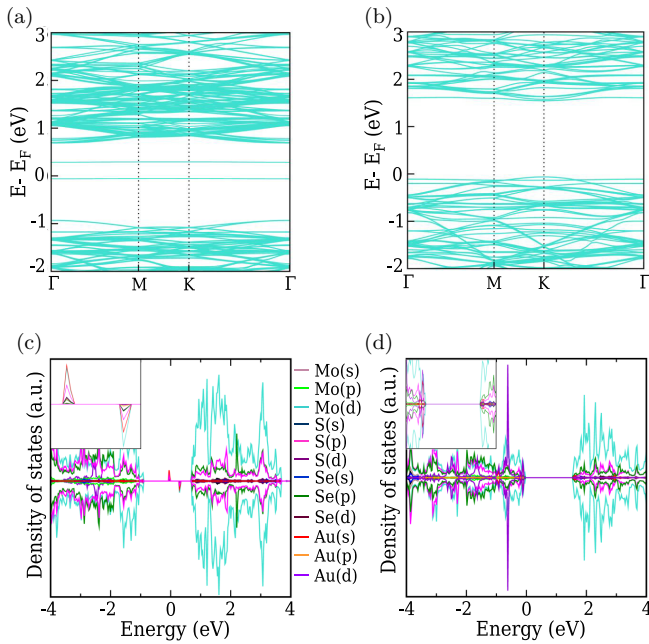


FIG. 5. First-principles calculations. (a) and (b) Electronic band structures and (c) and (d) atom-projected partial density of states for the Au/MoSSe and Au₂/MoSSe hybrid configurations, respectively, where $n = 1$ and 2 refer to one Au NC and two Au NCs. The insets in (c) and (d) represent a zoomed-in view of the corresponding forbidden band gap regions.

the calculated area coverage derived from AFM images. The position of the longitudinal mode is closer to the 633 nm laser excitation. From Fig. S6(b) [31], we notice an absorption peak at 760 nm for pristine MoSSe corresponding to the excitonic transition of MoSSe. Compared with the bare sample after introduction of Au NCs, absorption of MoSSe decreases in the beginning, attributed to strong coupling between MoSSe and Au after hybrid formation and charge transfer from MoSSe to Au [51]. Then, it increases again with growth times. But absorption of Au NCs is enhanced monotonically. Both quenching and enhancement phenomena are in agreement with our PL observations. The observed mismatch between the PL emission and absorption peaks associated with Au NCs may be attributed to variations in size and density, which may differ depending on the substrate used, i.e., SiO₂/doped Si, MoSSe/SiO₂/doped Si, and a glass slide [52,53].

Our first-principles calculations of electronic band structures based on DFT provide a qualitative understanding of the effects of Au NCs' adsorption on the pristine MoSSe monolayer. We computed the atom-projected pDOS for the hybrid systems, Au_{*n*}/MoSSe ($n = 1, 2$). Here, $n = 1$ refers to the adsorption of one Au NC on a pristine $6 \times 6 \times 1$ MoSSe monolayer, while, for $n = 2$, we double the adsorption of Au NCs on the pristine MoSSe monolayer. Upon adsorption of Au NCs [see Figs. 5(a) and 5(c)], midgap states are formed, primarily composed of Au *s* and Mo *d* orbitals, with a minimal contribution from other orbitals. In Au₁/MoSSe, the band edges are mainly derived from Mo *d* orbitals. Consequently, during the return from the conduction band of MoSSe, electrons become trapped in the midgap state of the hybrid

system, leading to nonradiative recombination. With an increase in the size of Au NCs, the contribution of Au *d* orbitals grows, shifting the midgap states of Au₁/MoSSe to lower energies in the case of Au₂/MoSSe. This shift eliminates states within the forbidden gap, resulting in a situation where the VBM in Au₂/MoSSe mainly arises from a hybridization of Mo *d*, Au *d*, and Au *s* orbitals, while the CBM is primarily attributed to Mo *d* orbitals. Thus, the Au₂/MoSSe system is a spin-unpolarized configuration with a direct band gap of approximately 1.61 eV at the *K* point [see Fig. 5(b)]. The pDOS plot [Fig. 5(d)] reveals the disappearance of midgap states, thereby reactivating the potential pathway for radiative recombination. Moreover, we observe a contribution from Au *d* orbitals at the band edges of the hybrid system Au₂/MoSSe which is absent in the previous case [Fig. 5(c)]. In Au₂/MoSSe, the VBM displays a significant contribution from filled Au *d* orbitals, resulting in substantial charge localization near the surface of the Au NCs and subsequently enhancing the local electric field.

To quantify the localized electric field in the vicinity of a metal surface, we performed a simulation using the COMSOL MULTIPHYSICS program. In this study, we focused on the scenario where Au NCs are relatively far apart, behaving essentially as a single NC with $D \sim 10$ nm (determined via AFM analysis). We calculated the magnitude of the localized electric field for excitation wavelengths of 488 and 633 nm, which are represented as color plots in Figs. 6(a) and 6(e) and 6(b) and 6(f), respectively. Subsequently, we conducted simulations to investigate the localized electric field as the size [Figs. 6(c) and 6(g)] and density [Figs. 6(d) and 6(h)] of Au NCs increased, resulting in reduced inter-NC distances, as determined by AFM analysis (Figs. S2(d) and S2(f) [31]). Due to computational constraints, we limited our analysis to a two-NC system (i.e., a dimer) with decreasing inter-NC distances. Our results demonstrate that the role of the localized electric field becomes more pronounced with increasing NC size, aligning with our observations from PL enhancement behavior and DFT-based microscopic analysis [Figs. 5(b) and 5(d)]. Additionally, our simulations reveal that the enhancement of the localized electric field under 633 nm excitation exceeds that under 488 nm excitation due to resonance effects, consistent with the trends depicted in Figs. 4(a) and S4(c) [31], respectively.

The experimental results with the insights derived from the theoretical and simulation approaches culminate in a coherent depiction elucidated through a schematic model in Fig. 7. The right panels of Figs. 7(a)–7(c) display the pristine MoSSe and Au/MoSSe hybrids under laser excitation, and the left panels illustrate the recombination pathways in MoSSe before and after coupling with Au NCs. Following the introduction of Au NCs onto MoSSe, the interplay between nonradiative recombination in the presence of midgap states [process 3 in Fig. 7(b)] and charge transfer from MoSSe to Au [process 4 in Fig. 7(b)] precipitates the phenomenon of quenching in optical properties within the hybrid system [Fig. 7(b)]. Subsequent to the disappearance of midgap states [Fig. 7(c)] and the evolution of the geometrical parameters of the Au NCs, the LSPR effect engenders enhancement of the optical properties for both MoSSe and Au NCs within the hybrid, as depicted in Fig. 7(c).

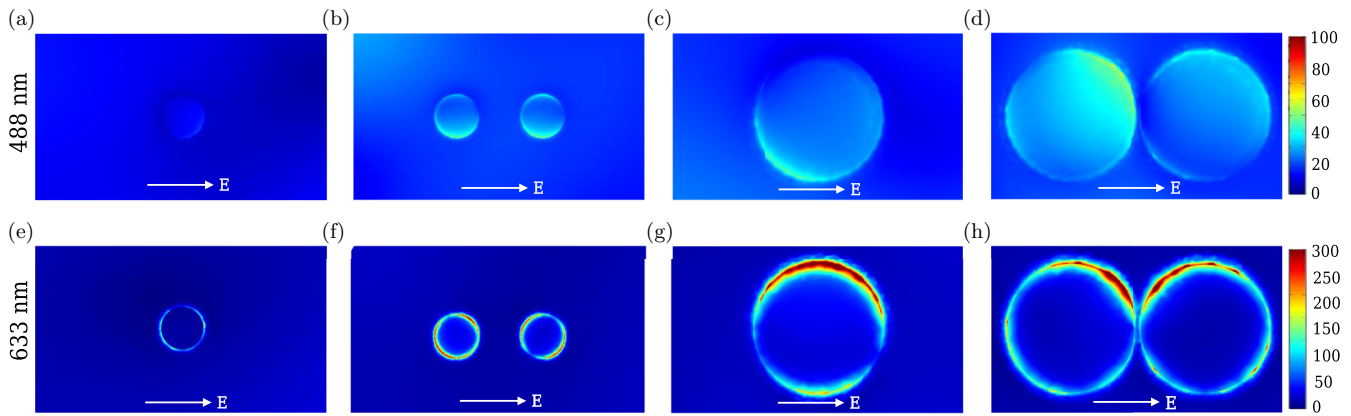


FIG. 6. Simulation of the EM field distribution in Au/MoSSe hybrids. (a) and (e) Single Au NC with a diameter D of 10 nm, (b) and (f) two identical Au NCs with $D = 10$ nm and a gap of 5 nm, (c) and (g) a single Au NC ($D = 30$ nm) and (d) and (h) two identical Au NCs ($D = 30$ nm) with a gap of 1 nm on MoSSe under 488 and 633 nm excitations, respectively. Here, E represents the direction of the incident EM field.

To gain deeper insight into the coupling effects between the Au NCs and MoSSe, we conducted Raman spectroscopy measurements on all hybrid samples, including Sample 1, using a 633 nm laser excitation. This wavelength was chosen due to the significant enhancement observed in PL emission upon its excitation. The color plot in Fig. S7(a) presents a clear depiction of the modulation in Raman mode intensity [31]. Importantly, we did not observe substantial peak shifts upon the introduction of Au NCs onto the MoSSe, indicating the absence of significant strain within the hybrid system [46]. Following the initial decrease in the intensity of all Raman modes, a pronounced enhancement in their intensity became evident after Sample 4 (Fig. S7(b) [31]). This quenching phenomenon can be attributed to the charge transfer process from MoSSe to

Au. Specifically, the photoexcited electron is efficiently transferred from MoSSe to Au before undergoing electron-phonon scattering [23]. The enhancement in Raman intensity can be understood by the close alignment between the plasmonic energy of the Au NCs and the energy associated with the 633 nm laser (1.96 eV). The resonance effect leads to a strong localized EM field in the proximity of the Au NCs, intensifying the Raman signal of MoSSe through surface-enhanced Raman scattering. Among all the Raman peaks of MoSSe, the E_2^2 and E_1^1 modes exhibit greater sensitivity towards plasmon coupling. These findings shed light on the coupling between the plasmon and the phonon in the Au/MoSSe hybrid system, offering valuable insights for the design and optimization of such hybrid structures for various optoelectronic applications.

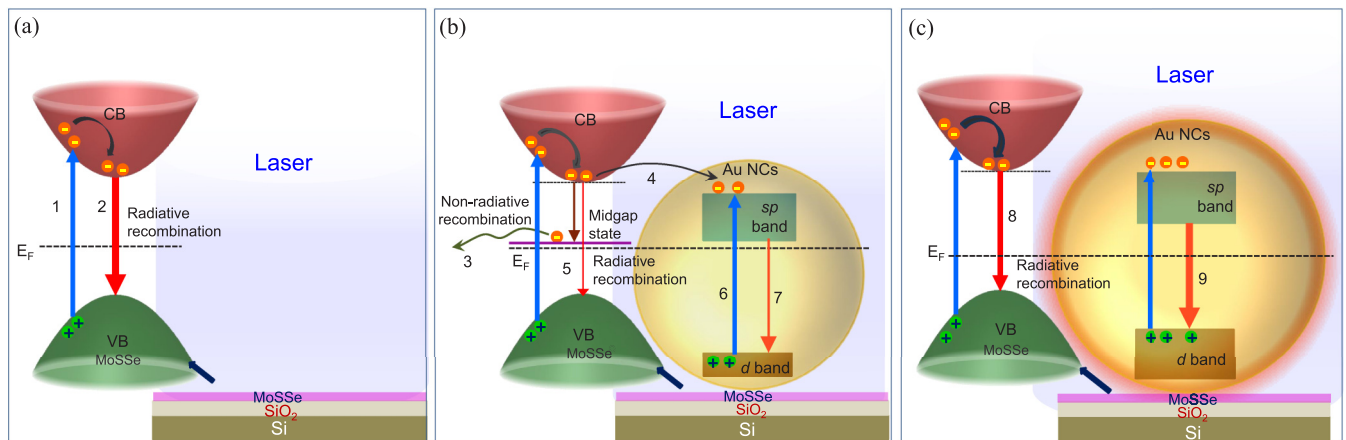


FIG. 7. Schematic presentation of the underlying mechanism. (a)–(c) depict recombination pathways in pristine MoSSe and Au ($D \sim 10$ nm)/MoSSe and Au ($D \sim 30$ nm)/MoSSe hybrids, respectively. The right panels show laser-irradiated pristine MoSSe and hybrids, whereas the left panels depict the modulation of the recombination pathways in MoSSe without and with Au NCs. (1) Absorption of the incident laser beam (blue arrow) by pristine MoSSe. (2) Emission through radiative recombination (red arrow). (3) The presence of the midgap state (purple line) causes nonradiative recombination (brown arrow). (4) After hybrid formation, charge transfer from MoSSe to Au starts. (5) Radiative recombination of the active sample decreases. (6) Absorption of the incident laser beam (blue arrow) by Au NCs. (7) Emission from Au NCs due to radiative recombination between d -band holes and sp -band electrons. (8) The disappearance of the midgap state and activation of the LSPR effect due to the increasing size of Au NCs again result in enhancement of radiative recombination, promoting higher PL emission. (9) Due to the size evolution of Au NCs in the hybrid system, the intensity of the emission of Au NCs also increases.

IV. CONCLUSION

In summary, we reported a strategy to efficiently modify exciton-plasmon coupling of TMDCs by integrating Au NCs over MoSSe. The Au/MoSSe hybrid exhibits a broad emission spectrum spanning from the UV-VIS to NIR region, making it a promising candidate for broadband optoelectronic applications. By introducing size-dependent Au NCs over MoSSe, we successfully achieved quenching due to charge transfer as well as subsequent enhancement in optical properties. Additionally, our theoretical investigation sheds light on the role of midgap electronic states, resulting in nonradiative dissociation of emission in the optical properties of Au/MoSSe hybrids. After the evolution of the size of Au NCs, the LSPR effect becomes a crucial factor for enhancing the optical properties. Thus, we presented an approach to engineer the exciton-plasmon interaction within an optically active TMDC/plasmon hybrid. These findings hold significant importance for improving the metal-semiconductor interface for device applications. Furthermore, this work has

expanded our understanding of the vibrational properties of plasmon-mediated systems, offering a fresh perspective in this field.

ACKNOWLEDGMENTS

We thank Dr. Prasanna Kumar Mondal, Surendranath College, Kolkata, for helping us to perform the simulation using the COMSOL MULTIPHYSICS program. C.N. acknowledges the INSPIRE Fellowship Programme, the Department of Science & Technology, Government of India, for granting her a research fellowship with Registration No. IF180057. S. Masanta expresses gratitude to the Council of Scientific & Industrial Research (CSIR), India, for the financial support provided through the NET-SRF award [File No. 09/015(0531)/2018-EMR-I]. S. Monga and S. Bhattacharya acknowledge the High Performance Computing (HPC) facility at IIT Delhi for computational resources. A.S. acknowledges financial support from the Science and Engineering Research Board (SERB), India (File No. EMR/2017/002107).

-
- [1] Y.-J. Kim, Y. Lee, W. Choi, M. Jang, W.-W. Park, K. Kim, Q.-H. Park, and O.-H. Kwon, Two-dimensional matter using strong light-matter interactions, *Nano Lett.* **23**, 3645 (2023).
- [2] P. G. Zotev, Y. Wang, L. Sortino, T. Severs Millard, N. Mullin, D. Conteduca, M. Shagar, A. Genco, J. K. Hobbs, T. F. Krauss *et al.*, Transition metal dichalcogenide dimer nanoantennas for tailored light-matter interactions, *ACS Nano* **16**, 6493 (2022).
- [3] A. M. Jones, H. Yu, J. R. Schaibley, J. Yan, D. G. Mandrus, T. Taniguchi, K. Watanabe, H. Dery, W. Yao, and X. Xu, Excitonic luminescence upconversion in a two-dimensional semiconductor, *Nat. Phys.* **12**, 323 (2016).
- [4] Z. Sun, J. Gu, A. Ghazaryan, Z. Shotan, C. R. Consideine, M. Dollar, B. Chakraborty, X. Liu, P. Ghaemi, S. K'ena-Cohen *et al.*, Optical control of room-temperature valley polaritons, *Nat. Photon.* **11**, 491 (2017).
- [5] K. F. Mak, C. Lee, J. Hone, J. Shan, and T. F. Heinz, Atomically thin MoS₂: A new direct-gap semiconductor, *Phys. Rev. Lett.* **105**, 136805 (2010).
- [6] A. Splendiani, L. Sun, Y. Zhang, T. Li, J. Kim, C. Y. Chim, G. Galli, and F. Wang, Emerging photoluminescence in monolayer MoS₂, *Nano Lett.* **10**, 1271 (2010).
- [7] Y. Lee, J. D. S. Forte, A. Chaves, A. Kumar, T. T. Tran, Y. Kim, S. Roy, T. Taniguchi, K. Watanabe, A. Chernikov *et al.*, Boosting quantum yields in two-dimensional semiconductors via proximal metal plates, *Nat. Commun.* **12**, 7095 (2021).
- [8] O. Salehzadeh, N. H. Tran, X. Liu, I. Shih, and Z. Mi, Exciton kinetics, quantum efficiency, and efficiency droop of monolayer MoS₂ light-emitting devices, *Nano Lett.* **14**, 4125 (2014).
- [9] J. Duan, P. Chava, M. Ghorbani-Asl, Y. Lu, D. Erb, L. Hu, A. Echresh, L. Rebohle, A. Erbe, A. V. Krasheninnikov *et al.*, Self-driven broadband photodetectors based on MoSe₂/FePS₃ van der Waals n-p type-II heterostructures, *ACS Appl. Mater. Interfaces* **14**, 11927 (2022).
- [10] V. Dhyani, P. Dwivedi, S. Dhanekar, and S. Das, High performance broadband photodetector based on MoS₂/porous silicon heterojunction, *Appl. Phys. Lett.* **111**, 191107 (2017).
- [11] S. Masanta, C. Nayak, S. Maitra, S. Rudra, D. Chowdhury, S. Raha, M. Pradhan, B. Satpati, P. Pal, and A. Singha, Engineering multifunctionality in MoSe₂ nanostructures via strategic Mn doping for electrochemical energy storage and photosensing, *ACS Appl. Nano Mater.* **6**, 5479 (2023).
- [12] Y. Liu, N. O. Weiss, X. Duan, H. C. Cheng, Y. Huang, and X. Duan, Van der Waals heterostructures and devices, *Nat. Rev. Mater.* **1**, 16042 (2016).
- [13] J. Jiang, T. Xu, J. Lu, L. Sun, and Z. Ni, Defect engineering in 2D materials: Precise manipulation and improved functionalities, *Research* **2019**, 4641739 (2019).
- [14] Q. Liang, Q. Zhang, X. Zhao, M. Liu, and A. T. S. Wee, Defect engineering of two-dimensional transition-metal dichalcogenides: Applications, challenges, and opportunities, *ACS Nano* **15**, 2165 (2021).
- [15] K. S. Novoselov, A. Mishchenko, A. Carvalho, and A. H. C. Neto, 2D materials and van der Waals heterostructures, *Science* **353**, aac9439 (2016).
- [16] S. Li, R. Ai, K. K. Chui, Y. Fang, Y. Lai, X. Zhuo, L. Shao, J. Wang, and H.-Q. Lin, Routing the exciton emissions of WS₂ monolayer with the high-order plasmon modes of Ag nanorods, *Nano Lett.* **23**, 4183 (2023).
- [17] X. Liu, J. Yi, S. Yang, E. C. Lin, Y. J. Zhang, P. Zhang, J. F. Li, Y. Wang, Y. H. Lee, Z. Q. Tian *et al.*, Nonlinear valley phonon scattering under the strong coupling regime, *Nat. Mater.* **20**, 1210 (2021).
- [18] S. S. Singha, D. Nandi, T. S. Bhattacharya, P. K. Mondal, and A. Singha, Photoluminescence modulation due to conversion of trions to excitons and plasmonic interaction in MoS₂-metal NPs hybrid structures, *J. Alloys Compd.* **723**, 722 (2017).
- [19] S. S. Singha, D. Nandi, and A. Singha, Tuning the photoluminescence and ultrasensitive trace detection properties of few-layer MoS₂ by decoration with gold nanoparticles, *RSC Adv.* **5**, 24188 (2015).
- [20] Q. Yue, L. Wang, H. Fan, Y. Zhao, C. Wei, C. Pei, Q. Song, X. Huang, and H. Li, Wrapping plasmonic silver nanopar-

- ticles inside one-dimensional nanoscrolls of transition-metal dichalcogenides for enhanced photoresponse, *Inorg. Chem.* **60**, 4226 (2021).
- [21] P. K. Venuthurumilli, P. D. Ye, and X. Xu, Plasmonic resonance enhanced polarization sensitive photodetection by black phosphorus in near infrared, *ACS Nano* **12**, 4861 (2018).
- [22] P. Sriram, Y. P. Wen, A. Manikandan, K. C. Hsu, S. Y. Tang, B. W. Hsu, Y. Z. Chen, H. W. Lin, H. T. Jeng, Y. L. Chueh *et al.*, Enhancing quantum yield in strained MoS₂ bilayers by morphology-controlled plasmonic nanostructures toward superior photodetectors, *Chem. Mater.* **32**, 2242 (2020).
- [23] I. Abid, P. Benzo, B. Pécassou, S. Jia, J. Zhang, J. Yuan, J. Dory, O. Gauthier Lafaye, R. Péchou, A. Mlayah *et al.*, Plasmon damping and charge transfer pathways in Au@MoSe₂ nanostructures, *Mater. Today Nano* **15**, 100131 (2021).
- [24] S. Butun, S. Tongay, and K. Aydin, Enhanced light emission from large-area monolayer MoS₂ using plasmonic nanodisc arrays, *Nano Lett.* **15**, 2700 (2015).
- [25] T. S. Bhattacharya, S. Mitra, S. S. Singha, P. K. Mondal, and A. Singha, Tailoring light-matter interaction in WS₂-gold nanoparticles hybrid systems, *Phys. Rev. B* **100**, 235438 (2019).
- [26] S. Najmaei, A. Mlayah, A. Arbouet, C. Girard, J. Léotin, and J. Lou, Plasmonic pumping of excitonic photoluminescence in hybrid MoS₂-Au nanostructures, *ACS Nano* **8**, 12682 (2014).
- [27] Y. Zeng, W. Chen, B. Tang, J. Liao, J. Lou, and Q. Chen, Synergistic photoluminescence enhancement of monolayer MoS₂ via surface plasmon resonance and defect repair, *RSC Adv.* **8**, 23591 (2018).
- [28] I. Irfan, S. Golovynskyi, M. Bosi, L. Seravalli, O. A. Yeshchenko, B. Xue, D. Dong, Y. Lin, R. Qiu, B. Li *et al.*, Enhancement of Raman scattering and exciton/trion photoluminescence of monolayer and few-layer MoS₂ by Ag nanoprisms and nanoparticles: Shape and size effects, *J. Phys. Chem. C* **125**, 4119 (2021).
- [29] P. Viste, J. Plain, R. Jaffiol, A. Vial, P. M. Adam, and P. Royer, Enhancement and quenching regimes in metal-semiconductor hybrid optical nanosources, *ACS Nano* **4**, 759 (2010).
- [30] S. Masanta, C. Nayak, P. Agarwal, K. Das, and A. Singha, Monolayer graphene-MoSSe van der Waals heterostructure for highly responsive gate-tunable near-infrared sensitive broadband fast photodetector, *ACS Appl. Mater. Interfaces* **15**, 14523 (2023).
- [31] See Supplemental Material at <http://link.aps.org/supplemental/10.1103/PhysRevB.109.125306> for the computational details (Sec. I), the atom-projected partial density of states plot for pristine MoSSe (Sec. II), the typical 2D AFM representation (topography, histogram of size distributions, and phase images) of pristine MoSSe and hybrid samples (Sec. III), the PL study of Au NCs on the SiO₂/doped Si substrate (Sec. IV), extracted parameters from the PL study of Au/MoSSe hybrids under 488 nm excitation (Sec. V), PL studies of few-layer MoSSe samples before and after integrating with Au NCs under 488 nm excitation (Sec. VI), UV-VIS spectroscopy of MoSSe and Au/MoSSe samples (Sec. VII), and a study of the vibrational properties of MoSSe and Au/MoSSe hybrids under 633 nm excitation (Sec. VIII). It also contains Refs. [54–59].
- [32] A. Bera, A. Singh, Y. A. Sorb, R. N. Jenjeti, D. V. S. Muthu, S. Sampath, C. Narayana, U. V. Waghmare, and A. K. Sood, Chemical ordering and pressure-induced isostructural and electronic transitions in MoSSe crystal, *Phys. Rev. B* **102**, 014103 (2020).
- [33] M. Drüppel, T. Deilmann, P. Krüger, and M. Rohlfling, Diversity of trion states and substrate effects in the optical properties of an MoS₂ monolayer, *Nat. Commun.* **8**, 2117 (2017).
- [34] Z. Wang, L. Zhao, K. F. Mak, and J. Shan, Probing the spin-polarized electronic band structure in monolayer transition metal dichalcogenides by optical spectroscopy, *Nano Lett.* **17**, 740 (2017).
- [35] R. Kaupmees, H. P. Komsa, and J. Krustok, Photoluminescence study of B-trions in MoS₂ monolayers with high density of defects, *Phys. Status Solidi B* **256**, 1800384 (2019).
- [36] A. Mooradian, Photoluminescence of metals, *Phys. Rev. Lett.* **22**, 185 (1969).
- [37] D. Sivun, C. Vidal, B. Munkhbat, N. Arnold, T. A. Klar, and C. Hrelescu, Anticorrelation of photoluminescence from gold nanoparticle dimers with hot-spot intensity, *Nano Lett.* **16**, 7203 (2016).
- [38] J. Kern, A. Trügler, I. Niehues, J. Ewering, R. Schmidt, R. Schneider, S. Najmaei, A. George, J. Zhang, J. Lou *et al.*, Nanoantenna-enhanced light-matter interaction in atomically thin WS₂, *ACS Photon.* **2**, 1260 (2015).
- [39] S. I. Park and H. M. Song, Synthesis of prolate-shaped Au nanoparticles and Au nanoprisms and study of catalytic reduction reactions of 4-nitrophenol, *ACS Omega* **4**, 7874 (2019).
- [40] S. Boroviks, Z. H. Lin, V. A. Zenin, M. Ziegler, A. Dellith, P. A. D. Gonçalves, C. Wolff, S. I. Bozhevolnyi, J. S. Huang, and N. A. Mortensen, Extremely confined gap plasmon modes: when nonlocality matters, *Nat. Commun.* **13**, 3105 (2022).
- [41] C. Lumdee, B. Yun, and P. G. Kik, Gap-plasmon enhanced gold nanoparticle photoluminescence, *ACS Photon.* **1**, 1224 (2014).
- [42] O. A. Yeshchenko, V. V. Kozachenko, A. V. Tomchuk, M. Haftel, R. J. Knize, and A. O. Pinchuk, Plasmonic metasurfaces with tunable gap and collective SPR modes, *J. Phys. Chem. C* **123**, 13057 (2019).
- [43] Z. Q. Wu, J. L. Yang, N. K. Manjunath, Y. J. Zhang, S. R. Feng, Y. H. Lu, J. H. Wu, W. W. Zhao, C. Y. Qiu, J. F. Li *et al.*, Gap-mode surface-plasmon-enhanced photoluminescence and photoresponse of MoS₂, *Adv. Mater.* **30**, 1706527 (2018).
- [44] O. A. Yeshchenko, V. V. Kozachenko, Y. F. Liakhov, A. V. Tomchuk, M. Haftel, and A. O. Pinchuk, Surface plasmon resonance in electrodynamically-coupled Au NPs monolayer/dielectric spacer/Al film nanostructure: tuning by variation of spacer thickness, *Mater. Res. Express* **4**, 106401 (2017).
- [45] L. Jiang, T. Yin, Z. Dong, H. Hu, M. Liao, D. Allioux, S. J. Tan, X. M. Goh, X. Li, J. K. W. Yang *et al.*, Probing vertical and horizontal plasmonic resonant states in the photoluminescence of gold nanodisks, *ACS Photon.* **2**, 1217 (2015).
- [46] D. Lu, L. Du, K. Huang, X. Qi, B. Li, J. Zhong, and Y. Wang, Amplified local strain signal in strain-plasmonic coupled van der Waals heterostructures, *Phys. Rev. Appl.* **18**, 024003 (2022).
- [47] J. Shi, J. Zhu, X. Wu, B. Zheng, J. Chen, X. Sui, S. Zhang, J. Shi, W. Du, Y. Zhong *et al.*, Enhanced trion emission and carrier dynamics in monolayer WS₂ coupled with plasmonic nanocavity, *Adv. Opt. Mater.* **8**, 2001147 (2020).
- [48] K. A. Dahan, Y. Li, J. Xu, and C. Kan, Recent progress of gold nanostructures and their applications, *Phys. Chem. Chem. Phys.* **25**, 18545 (2023).

- [49] L. K. Sørensen, D. E. Khrennikov, V. S. Gerasimov, A. E. Ershov, S. P. Polyutov, S. V. Karpov, and H. Ågren, Nature of the anomalous size dependence of resonance red shifts in ultrafine plasmonic nanoparticles, *J. Phys. Chem. C* **126**, 16804 (2022).
- [50] W. T. Wu, C. H. Chen, C. Y. Chiang, and L. K. Chau, Effect of surface coverage of gold nanoparticles on the refractive index sensitivity in fiber-optic nanoplasmonic sensing, *Sensors* **18**, 1759 (2018).
- [51] R. Sharma, J. Aneesh, R. K. Yadav, S. Sanda, A. R. Barik, A. K. Mishra, T. K. Maji, D. Karmakar, and K. V. Adarsh, Strong interlayer coupling mediated giant two-photon absorption in MoSe₂/graphene oxide heterostructure: Quenching of exciton bands, *Phys. Rev. B* **93**, 155433 (2016).
- [52] M. D. Malinsky, K. L. Kelly, G. C. Schatz, and R. P. Van Duyne, Nanosphere lithography: Effect of substrate on the localized surface plasmon resonance spectrum of silver nanoparticles, *J. Phys. Chem. B* **105**, 2343 (2001).
- [53] G. Xu, Y. Chen, M. Tazawa, and P. Jin, Influence of dielectric properties of a substrate upon plasmon resonance spectrum of supported Ag nanoparticles, *Appl. Phys. Lett.* **88**, 043114 (2006).
- [54] P. Hohenberg and W. Kohn, Inhomogeneous electron gas, *Phys. Rev.* **136**, B864 (1964).
- [55] W. Kohn and L. J. Sham, Self-consistent equations including exchange and correlation effects, *Phys. Rev.* **140**, A1133 (1965).
- [56] M. Gajdoš, K. Hummer, G. Kresse, J. Ohnüller, and F. Bect, Linear optical properties in the projector-augmented wave methodology, *Phys. Rev. B* **73**, 045112 (2006).
- [57] P. E. Blöchl, Projector augmented-wave method, *Phys. Rev. B* **50**, 17953 (1994).
- [58] G. Kresse and J. Furthmüller, Efficiency of ab-initio total energy calculations for metals and semiconductors using a plane-wave basis set, *Comput. Mater. Sci.* **6**, 15 (1996).
- [59] J. P. Perdew, K. Burke, and M. Ernzerhof, Generalized gradient approximation made simple, *Phys. Rev. Lett.* **77**, 3865 (1996).